

MIT Open Access Articles

Scattering of long wavelengths into thin silicon photovoltaic films by plasmonic silver nanoparticles

The MIT Faculty has made this article openly available. **Please share** how this access benefits you. Your story matters.

Citation: Osgood, R. M., K. M. Bullion, S. A. Giardini, J. B. Carlson, P. Stenhouse, R. Kingsborough, V. Liberman, et al. "Scattering of Long Wavelengths into Thin Silicon Photovoltaic Films by Plasmonic Silver Nanoparticles." Edited by Oleg V. Sulima and Gavin Conibeer. Next Generation Technologies for Solar Energy Conversion V (October 3, 2014). © 2014 Society of Photo-Optical Instrumentation Engineers (SPIE).

As Published: <http://dx.doi.org/10.1117/12.2062268>

Publisher: SPIE

Persistent URL: <http://hdl.handle.net/1721.1/98068>

Version: Final published version: final published article, as it appeared in a journal, conference proceedings, or other formally published context

Terms of Use: Article is made available in accordance with the publisher's policy and may be subject to US copyright law. Please refer to the publisher's site for terms of use.



Scattering of long wavelengths into thin silicon photovoltaic films by plasmonic silver nanoparticles

R. M. Osgood III, K. M. Bullion, S. A. Giardini, J. B. Carlson, P. Stenhouse
US Army Natick Soldier Research Development and Engineering Center,
Natick, MA 01760

R. Kingsborough, V. Liberman, L. Parameswaran, M. Rothschild
MIT Lincoln Laboratory, Lexington, MA 02420

O. Miller, S. Kooi, J. Joannopoulos
Institute for Soldier Nanotechnologies, Massachusetts Institute of Technology,
Cambridge, MA 02139

F. Jeffrey, S. Braymen
PowerFilm Inc., Ames, IA 80401

H. Singh Gill, J. Kumar
Physics Department
University of Massachusetts – Lowell
Lowell, MA 01854

ABSTRACT

Nanoparticles and nanostructures with plasmonic resonances are currently being employed to enhance the efficiency of solar cells.¹⁻³ Ag stripe arrays have been shown theoretically to enhance the short-circuit current of thin silicon layers.⁴ Monolayers of Ag nanoparticles with diameter $d < 300$ nm have shown strong plasmonic resonances when coated in thin polymer layers with thicknesses $< d$.⁵ We study experimentally the diffuse vs. specular scattering from monolayer arrays of Ag nanoparticles (spheres and prisms with diameters in the range 50 – 300 nm) coated onto the front side of thin ($100 \text{ nm} < t < 500 \text{ nm}$) silicon films deposited on glass and flexible polymer substrates, the latter originating in a roll-to-roll manufacturing process. Ag nanoparticles are held in place and aggregation is prevented with a polymer overcoat. We observe interesting wavelength shifts between maxima in specular and diffuse scattering that depend on particle size and shape, indicating that the nanoparticles substantially modify the scattering into the thin silicon film.

Key Words: Photovoltaics, flexible thin films, amorphous silicon, nanoparticles, scattering, absorption, diffuse scattering, specular reflectivity, efficiency enhancement, NIR/visible spectrum, optical properties.

1. INTRODUCTION

Photovoltaic thin films are currently the focus of research, because they have the advantage of being thin enough to prevent recombination (which lowers the output photocurrent), flexible, and inexpensive (films are deposited, not cut from large single crystals) – important for use in austere environments and in the developing world. An example of a flexible, thin photovoltaic film is presented in Figure 1. However, because the films are thin, absorption is low, especially at large

angles of incidence. Nanoparticles and nanostructures, located on the front surface of the photovoltaic film, are currently under investigation to scatter long-wavelength light and increase absorption in the photovoltaic thin film.



Figure 1: A kW-scale flexible photovoltaic thin film module, based on amorphous silicon (α -Si) – a Power Shade™ solar tent manufactured by PowerFilm, Inc. (http://www.powerfilmsolar.com/military/products__systems/power-packs-and-high-power-solar/).

Energy conversion efficiency in bulk (e.g., crystalline silicon) solar cells has been increased by enhancing scattering through texturing the front and/or back sides of the solar cell. Such texturing requires micron-size features that are inapplicable to novel, flexible thin-film solar cells whose active area is thinner than one micrometer. Introducing small-scale plasmonic structures at the back surface of the solar cell has also produced efficiency improvements,² but these structures may be difficult to introduce into flexible thin films manufactured on a large-area plastic substrate, especially if high temperatures are required during the process of depositing the plasmonic structures and/or the thin photovoltaic film whose efficiency requires enhancement.

The conversion efficiency of advanced photovoltaic cells can be increased by incorporating metallic nanoparticles into a host polymer layer at the front (light-collecting side) of the thin photovoltaic film, provided that the particles scatter light into the photovoltaic active region (the intermediate field regime for silicon and other indirect band gap materials) and/or plasmonically enhance the absorption of incident visible/near-infrared light through near-field effects in the adjacent near-field regime.^{1,3} Metallic nanoparticles, and other metallic nanostructures having plasmonic resonances, have been shown to enhance the absorption of organic photovoltaic thin films as well.⁶ Figure 2 shows an interesting case where the efficiency of a polymeric organic photovoltaic solar cell has been increased due to addition of Ag nanoparticles, apparently due to

enhanced absorption by the polymer photovoltaic film (perhaps due to nanoparticle-enhanced scattering), and not just to a reduction in the series resistance.⁷

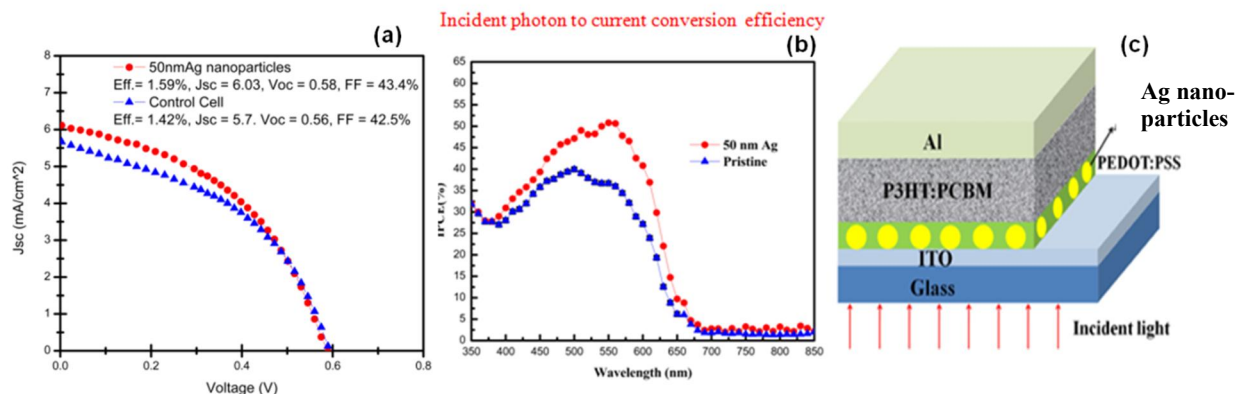


Figure 2: (a) Short-circuit current density J_{sc} vs. applied voltage for a P3HT:PCBM solar cell with (red curve) and without (blue curve) 50 nm Ag nanoparticles added to the electron-blocking PEDOT:PSS layer. (b) Internal photon-to-charge conversion efficiency shows higher quantum efficiency for the nanoparticle-bearing sample. (c) Sample layout showing addition of nanoparticles.

Another approach for increasing the efficiency of thin-film solar cells involves dielectric nanostructures as front-side scatterers. Such scatterers include high-index nanostructures, such as TiO_2 (index of refraction $n \sim 2.6$)⁸ or silicon ($n \sim 3.5$ in the near-infrared). In the quasi-static limit, however, for very small particles (diameter 30 nm or less), plasmonic particles are expected to scatter more efficiently, because their dielectric constant is large and negative (in contrast to dielectric particles). For larger particles, such as those examined in this study, it is important that the dielectric constant be large – both metal and silicon particles represent good options for scattering to enhance, potentially, long-wavelength absorption by the underlying silicon thin film. In this study, we focused attention on enhancing scattering with Ag nanoparticles.

2. EXPERIMENTAL – NANOPARTICLE AND MONOLAYER SYNTHESIS

Plasmonic nanoparticles exhibit scattering and absorption that can be designed by choice of nanoparticle geometry, size, shape, and material. For this study, we used two types of custom-synthesized silver nanoparticles. Near-spherical icosahedral single-crystal, surfactant-free Ag nanoparticles (SNPs), having diameters of 50 nm, 120 nm, and 300 nm, were obtained from Prof. Chumanov's group at Clemson University, and formed into monolayers that have been extensively studied both at Clemson University and the US Army NSRDEC.⁵ While these samples don't have maximal nanoparticle coverage, we describe them with the term "monolayer" because they have large fill factors and are close to a monolayer in coverage, as shown in Figure 3. Briefly, SNPs suspended in water were received and rolled on a roller machine in vials with substrates that were previously coated with ultrathin layers of poly(4-vinylpyridine). As explained in Reference 5, this procedure affixed the SNPs to the substrates, which were next taken through a process of sequential mixing steps to replace the water with polymethyl methacrylate (PMMA), while keeping the SNPs, adhered to the substrate, wet in order to prevent aggregation. Finally, the substrates were placed on a spincoater and spun (with a few additional drops of PMMA) to remove the excess PMMA and dry a nanoparticle-bearing

PMMA coating, whose final thickness was roughly equal to the nanoparticle's radius. This procedure produced films with near-monolayer coverage (see Fig. 3).

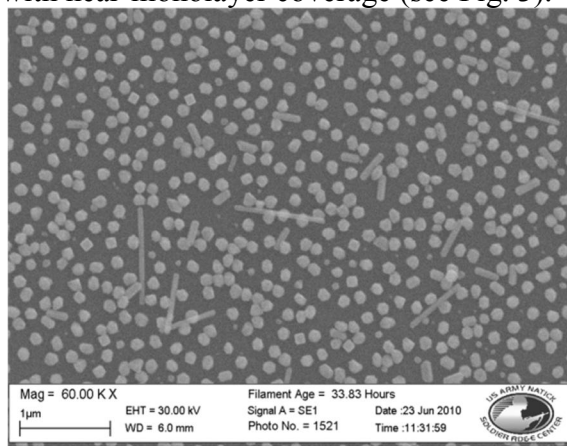


Figure 3: Plan view electron microscopy image of typical monolayer coating of 120 nm diameter SNPs in PMMA on silicon.

MIT Lincoln Laboratory (MITLL) synthesized silver nanoprisms (NP) according to the method of Yang and coworkers.⁹ MITLL also deposited thin films of amorphous silicon (α -Si) 100 nm, 200 nm, 300 nm, 400 nm, and 500 nm in thickness on glass, and characterized these films' indices of refraction.

MITLL's custom-synthesized nanoprisms were terminated with polyvinylpyrrolidone (PVP), which allowed for facile dispersion in isopropanol solvents. Two different size fractions of nanoprisms, labeled "small" and "large", were isolated and characterized. The UV-vis-NIR extinction spectra of the custom-synthesized nanoprisms is shown in Figure 4. The suspensions of small particles appeared purple red in color, while the large particles were grey and appeared milky, indicating the presence of increasing contribution of scattering to the absorption properties of the suspension. The "small" nanoprisms were mainly flat and disk-shaped, with diameters of less than 100 nm and a thickness of 35 nm, although there were some larger triangular shaped nanoprisms with edge lengths of approximately 150 nm (left inset of Figure 4). The "large" nanoprisms were more irregularly shaped flat particles with the same thickness as the smaller particles with much larger particle sizes of >500 nm (right inset of Figure 4). The irregular shapes can be thought of as multiple edge-fused nanoprisms, as was observed by Yang and co-workers.⁹

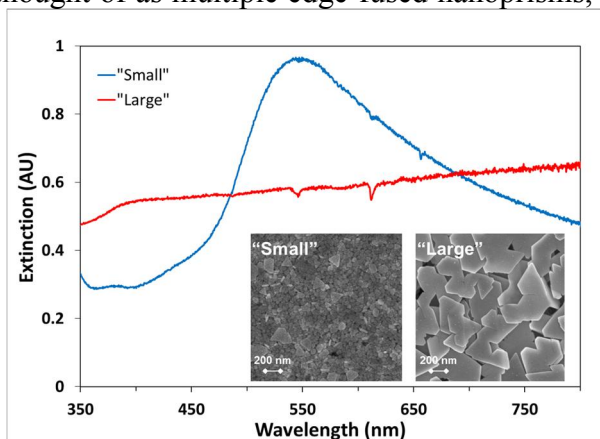


Figure 4: UV-vis spectra of custom synthesized nanoprism suspensions in water. Insets show SEM images of the "Small" and "Large" nanoprism fractions.

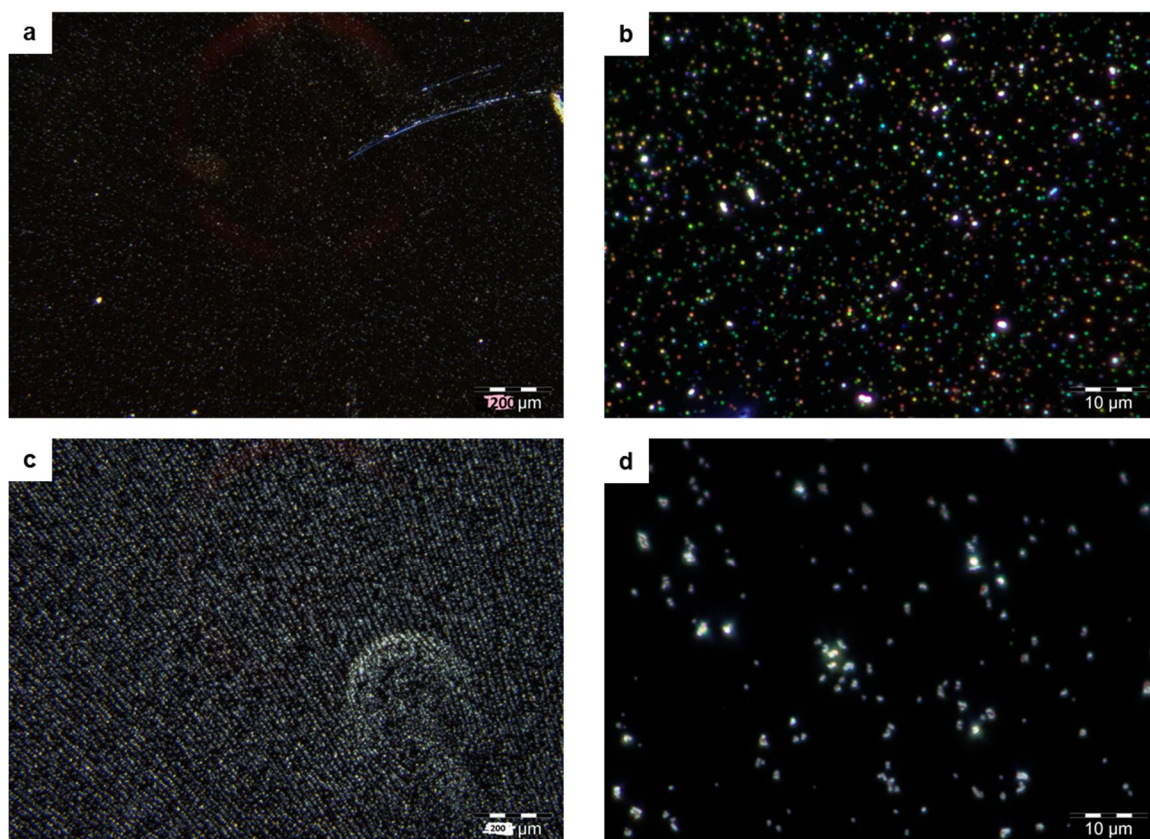


Figure 5. Dark field microscopy images of PVP:NP = 4:1 samples on 300 nm a-Si substrates. Images a-b show the “Small” particles and images c-d show the “Large” particles at 5x and 100x magnification.

Aqueous dispersions of the nanoprisms were transferred to isopropanol (IPA) for incorporation into polyvinylpyrrolidone (PVP) spin coating solutions. This involved gradually changing the composition of the dispersion solvent from 100% water to 100% IPA in a series of centrifugation and redispersion-via-sonication steps. Once the nanoprisms were in IPA, the nanoprisms were concentrated by centrifugation and a 10-mL solution of 3 wt. % PVP in IPA was added and the dispersion was redispersed via sonication. Thin films (~75 nm) were coated on solid substrates via spin coating at 8000 rpm for 45 sec. To examine the effects of different particle concentrations (“particle loading”), the nanoprisms recovered after synthesis and transfer to an IPA dispersion were split into four 2.5-mL fractions. Each set of nanoprisms was concentrated by centrifugation, the IPA removed, and then varying amounts of 3 wt. % PVP in IPA were added to create dispersions where the PVP:NP ratio varied from 0.5:1 to 4:1 relative to the standard PVP:NP ratio, designated as 1:1.

Polymer films with embedded nanoprisms were deposited onto α -Si/fused silica substrates via spin coating. The films were designed so that the thickness of the polymer film (75 nm) would result in a quasi-monolayer nanoprism arrangement and leave the nanoprisms encapsulated within a polymer matrix. The apparent distribution of the nanoparticles within the film was investigated by dark field microscopy. Low- and high-magnification images of these films in the areas where scattering measurements were performed are shown in Figure 5 for the PVP:NP = 4:1 samples. The high magnification images were analyzed to determine the apparent particle loading for each film, and the results were summarized in Table 1. As expected, the areal density of particles/ μm^2 in the spin-coated film decreased with decreasing particle loading.

Loading	“Small” Particles	“Large” Particles
0.5:1	1.54	0.36
1:1	1.25	0.14
4:1	0.74	0.06

Table 1: Apparent particle density per μm^2 , for three different PVP:NP ratios.

To understand the effect of scatter redirection in the presence of a high index substrate, we deposited (via e-beam evaporation at room temperature) films of amorphous silicon, with thicknesses $t = 100$ nm, 200 nm, 300 nm, 400 nm, and 500 nm, onto UV-grade fused silica substrates with area 1 square inch and thickness of 1 mm. The refractive indices of these amorphous silicon thin films were measured ellipsometrically, as illustrated in Figure 6 for the 300 nm thick α -Si films. PVP films with embedded nanoprisms, as well as PMMA films affixing SNPs with diameters of 50 nm, 120 nm, and 300 nm, were spin-coated onto the α -Si films on fused silica substrates. The PVP thickness (75 nm) was designed to result in a quasi-monolayer arrangement of nanoprisms, which, unlike the SNPs, were completely encapsulated within the polymer (PVP) matrix. In the absence of nanoparticles, the absorbance of a thin film stack, comprising a polymer film on a 300-nm thick amorphous silicon, was expected to be 50% at 780 nm wavelength, where angle-resolved scattering measurements were performed.

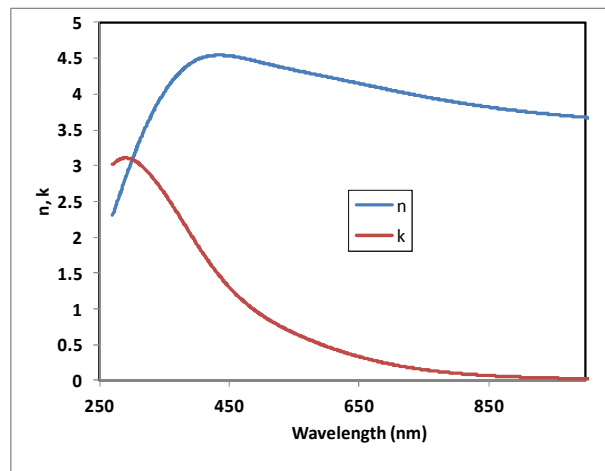


Figure 6. Optical constants of amorphous silicon films used in this study derived from spectroscopic ellipsometry measurements.

3. RESULTS – OPTICAL CHARACTERIZATION AND ANALYSIS

In order to quantitatively determine the potential for nanoparticle arrays to enhance the short-circuit current of α -Si thin films, we characterized both experimentally and theoretically the scattering from the nanoparticle monolayer array samples described in Section 2. Angle-resolved and angle-integrated measurements were both carried out, and compared to simulation. The latter experiment probed smaller areas with well-controlled angles of incidence and scattering, produced more detailed information about scattering from the arrays, and was more readily comparable to theory, but had a comparatively weaker signal that required a laser source and therefore was possible at one fixed wavelength (780 nm). The former experiment produced much larger signals, but was harder to analyze. Nevertheless, interesting trends were observed in

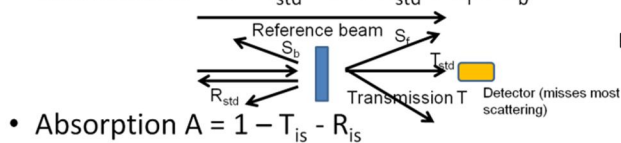
both experiments; in particular, the angle-integrated measurements showed strong sensitivity to the type of nanoparticle present in the array, indicating strong variations in scattered intensity from different nanoparticles.

Total integrated diffuse scattering measurements

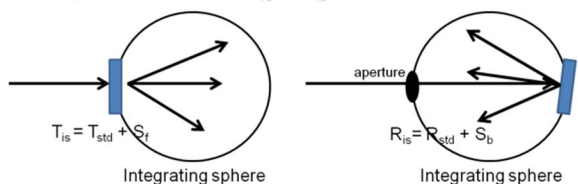
Angle-integrated scattering measurements were carried out by measuring the absorption and total integrated diffuse forward- and back-scattering, using a standard UV-vis-NIR spectrophotometer with integrating sphere accessory (Perkin-Elmer Lambda 900 spectrophotometer). Figure 7a schematically illustrates the method used for extracting scattering and specular reflectivity and transmission from the samples. Only the total integrated diffuse scattering (“TIDS”) - not angle-resolved scattering - could be measured using this method. In the standard spectrophotometer configuration, with no integrating sphere, only the specular transmission T_{std} could be measured. The total integrated backscattering signal S_b was obtained by normalizing the intensity propagating backwards from the sample to the intensity of the incident light. To measure S_b , a small window in the integrating sphere was removed to permit the specularly reflected beam to exit the integrating sphere. The specular reflectivity R_{std} could therefore be determined by repeating the same measurement without removal of this small window, and taking the difference. We found that sample roughness broadened the specularly reflected beam by a small amount, and as a result there was a small residual signal in S_b , in the absence of nanoparticles, which had the same dependence on wavelength (λ) as R_{std} . The forward scattering signal S_f was measured by subtracting T_{std} from the integrated forward scattering (“ T_{is} ” in Fig. 7a), and so even a sample without nanoparticles produced a small (~2%) residual S_f signal due to sample roughness, which had dependence on wavelength similar to that of T_{std} .

Because of the relatively high index of the a-Si substrate, nanoparticles were expected to preferentially scatter long-wavelength light into the absorbing α -Si films. However, the situation was complicated by the very strong Fabry-Perot resonances present in these thin films of α -Si, which are illustrated in Fig. 8 for a single 500 nm thick film of α -Si on glass. These resonances strongly influence the optical intermediate field, where distances are on the order of a wavelength.

- Extinction $X = 1 - T_{\text{std}} = A + R_{\text{std}} + S_f + S_b$



- Absorption $A = 1 - T_{\text{is}} - R_{\text{is}}$



- Extinction – absorption = $X - A = R_{\text{std}} + S_f + S_b$

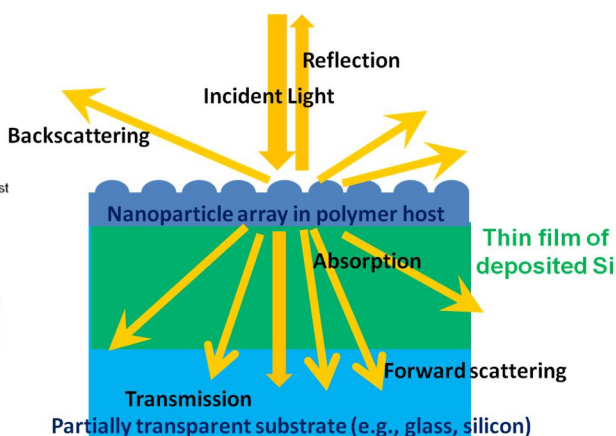


Figure 7: (a) Schematic illustration of the experimental method for measuring TIDS. Four measurements (T_{std} , T_{is} , R_{is} , and S_b), one of which (T_{std}) was made without the integrating sphere, determined four unknowns as a function of wavelength: S_b , S_f , T_{std} , and R_{std} . (b) Schematic diagram of TIDS optical measurements and samples investigated using the TIDS technique.

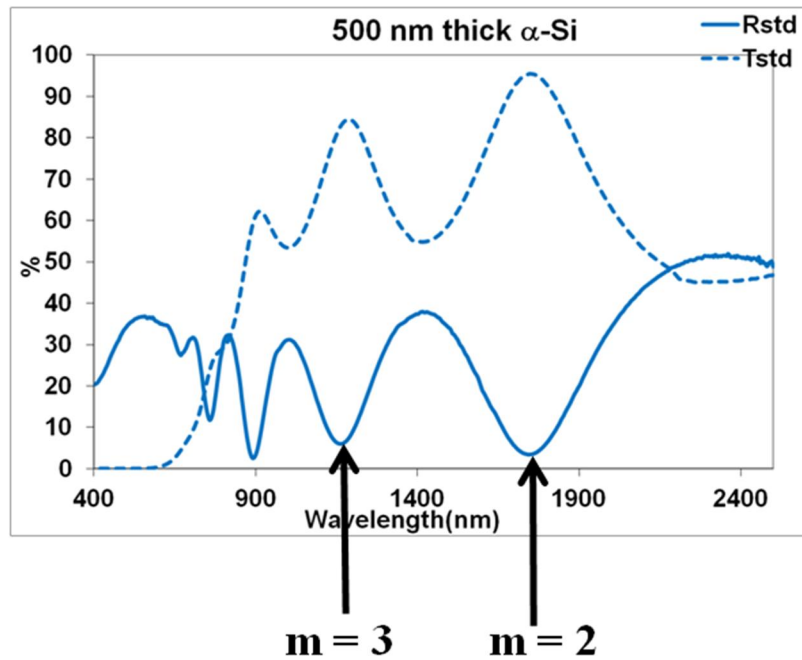


Figure 8. Experimental Fabry-Perot transmission and reflectivity resonances from a 500 nm α -Si film on glass. Vertical arrows indicate the $m = 2$ and 3 transmission maxima for resonances obeying the condition $m\lambda = n_{\text{Si}} d \cdot 2$.

TIDS measurements were carried out on control samples (no nanoparticles) and samples discussed in Section 2. Samples with arrays of “large” nanoprisms, and also 120 nm SNPs, exhibited a large spectral shift between the integrated backscattered intensity S_b and the reflected light R_{std} , and also between S_f and T_{std} , as shown in Figures 9 and 10. Arrays of “small” nanoprisms showed less of an effect, as also is shown in Fig. 9. The control sample, as discussed above, showed comparatively little shift, because for a control sample S_b and S_f were residual signals from sample roughness, and didn’t represent scattering from nanoparticles. Thus, for the control samples the peaks and valleys of S_b and R_{std} usually lined up with each other.

As shown in Fig. 11, the 50 nm diameter SNPs did not cause appreciable scattering, but instead absorbed short-wavelength light. This was expected because of the greater absorption vs. scattering cross-section for these smaller particles.⁵ Also as shown in Fig. 11, the 300 nm SNPs caused very large scattering effects, including a large backwards scattering component, so that S_b was larger than or equal to R_{std} . While these 300 nm SNPs will not effectively couple light into an underlying photovoltaic thin film at normal incidence, they produced a matte finish potentially useful for some applications, and may be useful for redirecting light at large angles of incidence. In conclusion, the scattering effects most relevant to photovoltaic thin film absorption were observed with 120 nm SNPs and the MITLL “large” nanoprisms – Ag particles with sizes in the 120 – 800 nm range.

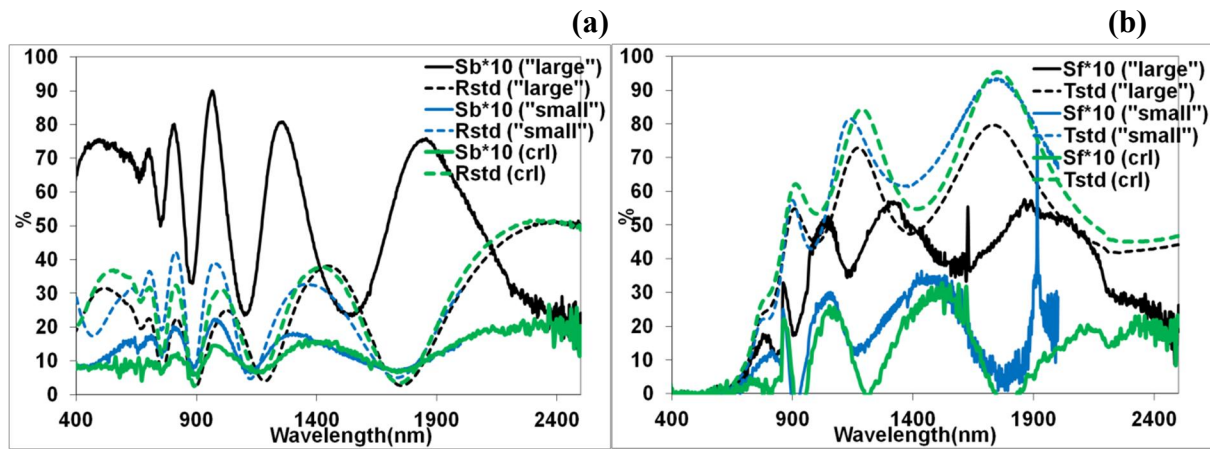


Figure 9: (a) Integrated backscattering S_b and specular reflectivity R_{std} , and (b) integrated forward scattering S_f and specular transmission T_{std} , as a function of wavelength for “large” and “small” nanoprisms and control sample (500 nm α -Si on glass). observed shift between S_b and R_{std} is observed in (a) for the “large” nanoprisms, but not for the control (“crl”) sample, which contained no nanoparticles.

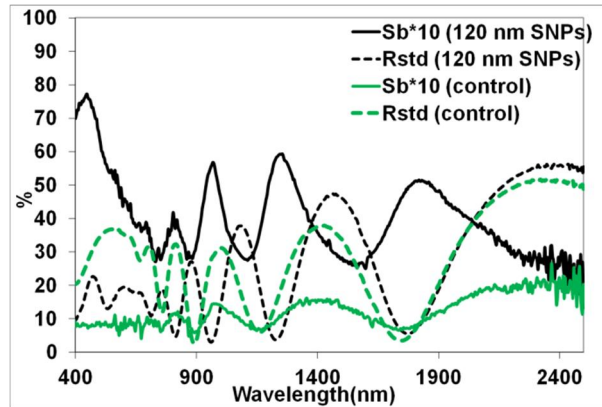


Figure 10: Shift in S_b with respect to R_{std} for 500 nm thick α -Si films coated with 120 nm SNPs.

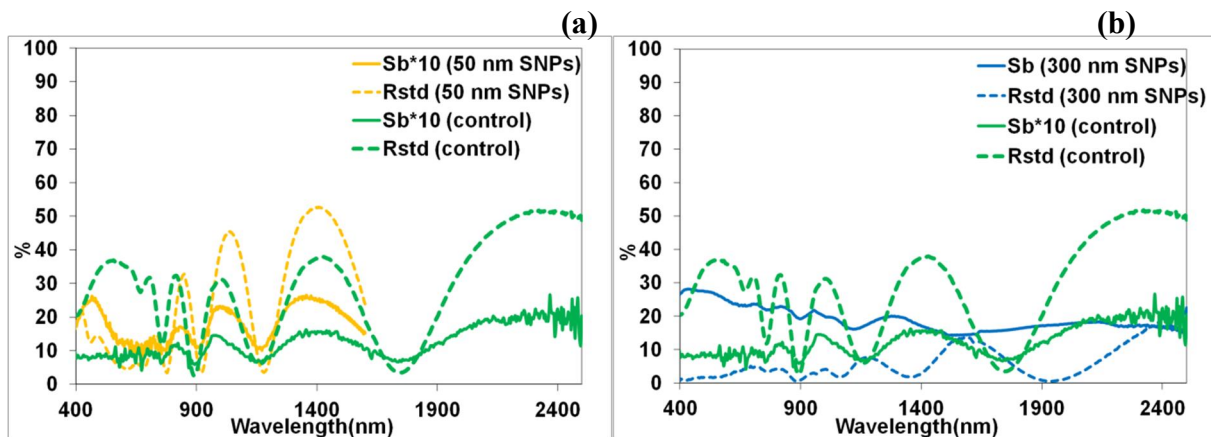


Figure 11: Shift in S_b with respect to R_{std} for 500 nm thick α -Si films coated with (a) 50 nm SNPs and (b) 300 nm SNPs. Note that 50 nm SNPs produce no shift, while for the 300 SNPs the specular reflectivity drops below S_b . Note also that S_b for the 300 nm SNPs in Fig. 11b is not multiplied by 10x, as it is in all the other figures.

We hypothesized that the spectral shift of S_b with respect to R_{std} , obtained experimentally by the TIDS measurement, might be due to a phase shift arising from the presence of Ag nanoparticles in the thin polymer layer on top of the 500 nm α -Si film, and therefore explainable by an effective medium theory. Ag's optical indices are very different from those of the surrounding polymer, with $n < 1$ for $\lambda < 2.5 \mu\text{m}$ and large (absorptive) k , so it seemed reasonable that this might create a phase shift in the diffusely scattered light. To verify this hypothesis, we calculated the reflectivity analytically for an effective medium with n reduced below PMMA's 1.43 and non-zero k (e.g., assuming "absorptive PMMA"). We assumed that Ag nanoparticles would act to reduce n and increase k in the polymer layer. The resulting reflectivity was much higher than what was observed experimentally – greater than 40% for all wavelengths if $n = 1.31$ and $k = 2$ were assumed. Given also that such a simple model could not explain diffuse scattering, we concluded that an effective medium theory could not explain the experimental observations, and instead focused on modeling optical/near-infrared scattering from nanoparticles.

The scattering of an individual nanoparticle was modeled using the finite difference time domain (FDTD) numerical algorithm, using optical indices for Ag from Palik.¹⁰ In order to simulate scattering from a single nanoparticle, the Total Field Scattered Field (TFSF) source was used, which automatically subtracts the incident fields from the total fields to yield only the scattered fields, which were used to obtain simulated values of S_b and S_f , as well as R_{std} and T_{std} . We ensured that the total scattered field depended only on the nanoparticle, and not on the size of the simulation. Using FDTD, we simulated a single 200 nm diameter, 40 nm thick Ag disk that represented the average "large" nanoprisms, as described in Section 2. These simulations predicted that the TIDS signal would reach maxima at wavelengths very similar to what was experimentally observed, as shown in Fig. 12a (albeit with a lower amplitude, than observed). Fig. 12b shows how the simulated spectral shift represented a constant frequency shift, as if there were a constant phase shift for light scattered instead of reflected.

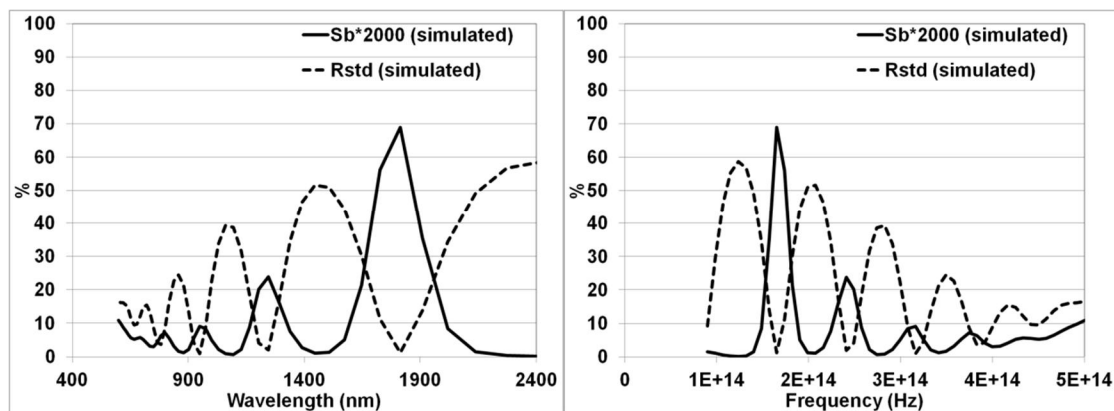


Figure 12: (a) Simulated S_b (multiplied by a factor of 2000) and R_{std} for a single Ag nanodisk on 500 nm thick α -Si film on glass (b) same, but plotted against frequency instead of wavelength.

We also examined α -Si films with different thicknesses, and found that 100 nm and 300 nm thick α -Si films showed a significant spectral shift between S_b and R_{std} for both "large" and

“small” nanoprisms, while for the 500 nm thick a-Si films, only the “large” nanoprisms exhibited a large spectral shift between S_b and R_{std} ; see Figs. 13-15.

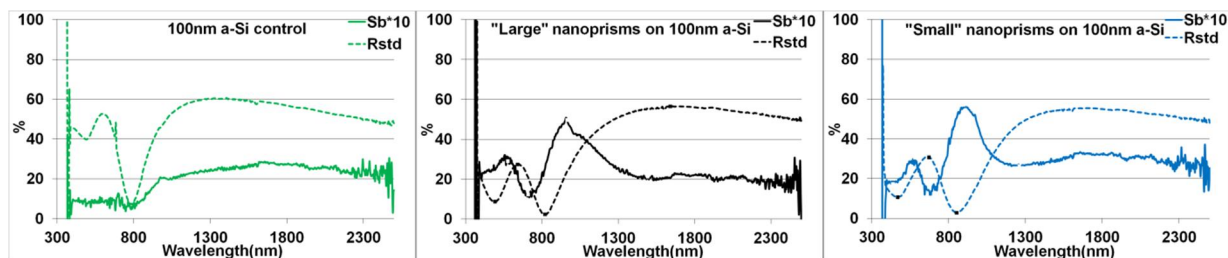


Figure 13: Shift in S_b with respect to R_{std} for 100 nm thick α -Si films: (a) control sample (b) coated with “large” nanoprisms and (c) coated with “small” nanoprisms.

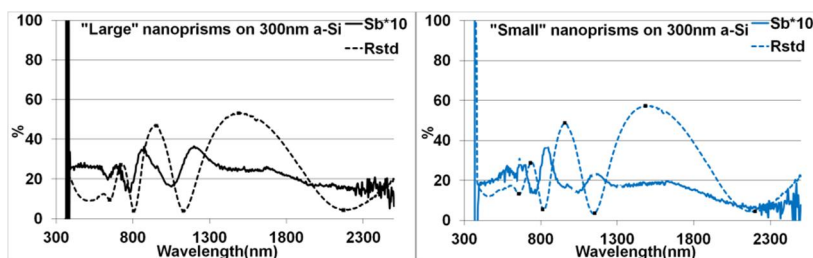


Figure 14: Shift in S_b with respect to R_{std} for 300 nm thick α -Si films: coated with (a) “large” and (b) “small” nanoprisms; no 300 nm thick α -Si control sample was available.

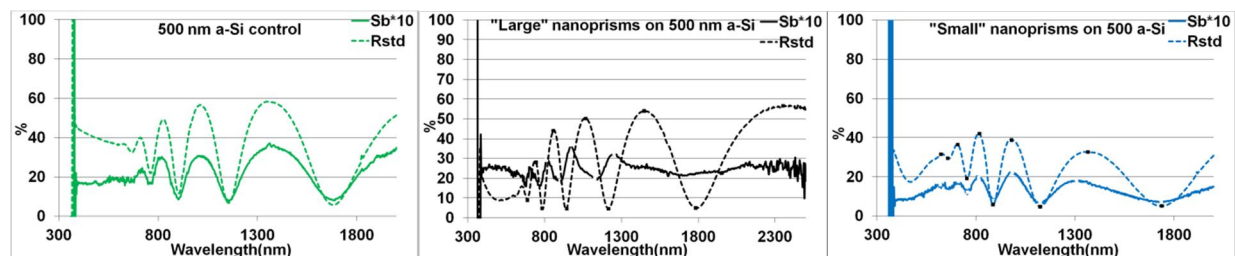


Figure 15: Shift in S_b with respect to R_{std} for 500 nm thick α -Si films (different sample from Fig. 9): (a) control sample (b) coated with “large” nanoprisms and (c) coated with “small” nanoprisms.

Angle-resolved scattering measurements

Angle-resolved scattering (ARS) measurements were also carried out with a 780 nm laser source. These ARS measurements allowed measurements of the angular distribution of scattering to compare to single-particle scattering models, and also allowed probing small regions on the size of the laser beam spot (2 mm x 2 mm). The ARS measurement geometry is shown schematically in Figure 16. A 780-nm diode laser was used for these measurements, both in order to specify the exact angle of the scattering, and because the signal was much lower than the total integrated signal measured in the TIDS experiment. The incident laser light passed through a half-wave plate so that data, for polarization both parallel and perpendicular to the scattering plane, could be acquired. In this study, normal incidence irradiation was used. Solid samples were mounted on a translation stage to allow measurements of spatial uniformity of scattering signal. The laser

spot size on the sample was 2x2 mm. The scattered light was apertured and focused onto a multimode fiber.

The angular acceptance of the detection set up was ± 3 degrees. The fiber assembly was mounted onto a rotary stage, which fully rotated 360° around the sample. Light passing through the fiber was coupled to a Si photodiode, after passing through a 780-nm bandpass filter to reject stray wavelengths. The detection setup was polarization-insensitive.

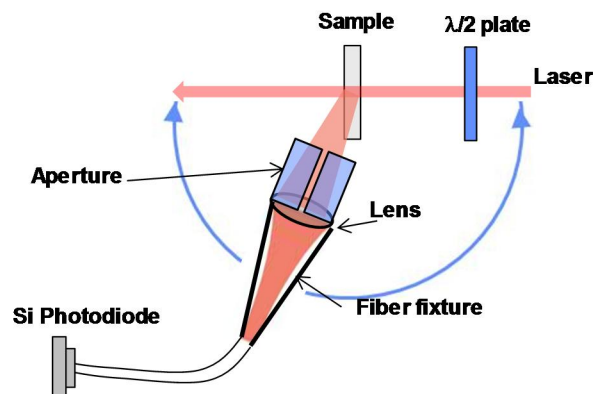


Figure 16. Schematic of the angle-resolved scattering setup.

For the measurements in this study, we defined 180° as the angle along the irradiation of light and 0° as the backscattered light. Near 90° , the edge of the sample blocked the signal and thus data could not be acquired. The data were acquired for two incident polarizations of the laser. All the polar data were acquired in the horizontal plane (azimuthal angle equaled zero).

Figures 17a and 17b show calibration measurements of the ARS setup performed with solid and liquid scattering standards, respectively. For this geometry, only backscatter data was acquired. In Fig. 17a, a solid thin sheet of Gore SpectralonTM material was analyzed. The ARS signature obeyed Lambert's cosine law well. In Fig. 17b, a suspension of monodisperse 40-nm diameter SiO₂ nanospheres in IPA was analyzed. The scattering signature was modeled in accordance with Mie theory for a spherical scatterer and agreed well with theory for both polarizations.

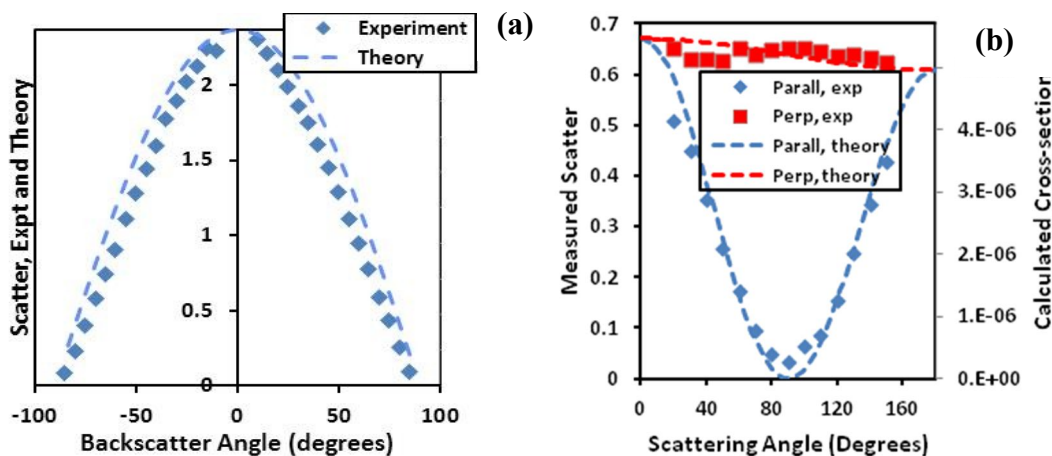


Figure 17: Calibration of the ARS setup. (a) Gore SpectralonTM solid sample (a Lambertian scatterer). (b) 40 nm colloidal SiO₂ nanoparticles suspended in isopropyl alcohol (IPA) in a cuvette. For both samples, excellent agreement with scattering theory predictions is observed.

Angle-resolved scattering measurements were acquired from samples with three different layer thicknesses of amorphous silicon and for both “large” and “small” nanoprism samples. These data are shown in Figure 18 for polarization perpendicular to the scattering plane, and should be compared to simulated scattering curves in Fig. 20 (specifically, the orange curve which represents 783 nm).

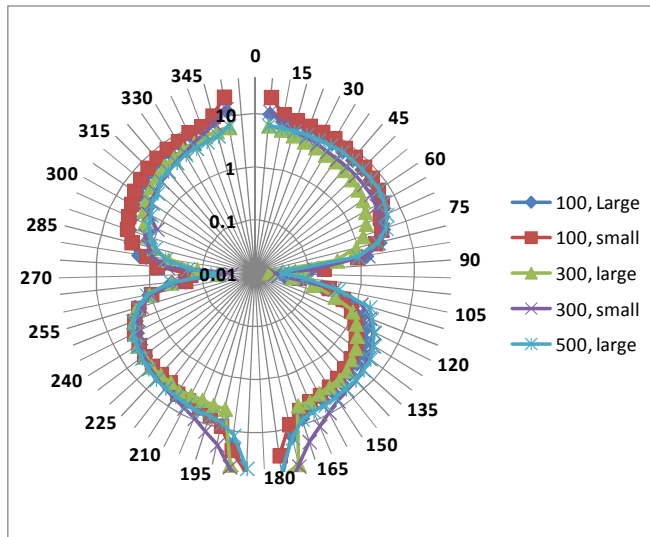


Figure 18. Experimental data (log scale) for angle resolved scattering for nanoprisms, performed at 780 nm in the plane perpendicular to the scattering plane. For each legend entry, the number refers to the thickness of the amorphous silicon layer, while “small” and “large” refer to the nanoprism sizes.

Single-particle angle-resolved simulations

In order to better explain the spectral shift observed between S_b and R_{std} (see Figure 19, which is the same as Fig. 9a) and the ARS data, we carried out a series of FDTD simulations of scattering from a single 200 nm diameter, 40 nm thick nanodisk, imitating the “large” nanoprisms, on a 500 nm α -Si film on glass at wavelengths corresponding to maxima and minima for S_b , also for polarization perpendicular to the scattering plane. The results of this model, displayed in Figure 20 on a log plot, predicted that the maxima of S_b corresponded to a much larger overall scattered intensity, and also that longer wavelengths scattered more. For the wavelengths representing minima of S_b (downwards-pointed arrows in Fig. 19 – for example, 1.51 μm), most of the light was scattered in the forward direction (e.g., through the substrate) and therefore the lower half of Fig. 20 contains larger scattering intensities. However, for the wavelengths that maximized S_b , the light was more evenly divided between the forward and backwards directions. Modeled angular scattering effects are shown in Figure 20 for five representative wavelengths, using the same angular definitions as in Figure 18, where $90^\circ < \theta < 270^\circ$ represents light propagating in the forward direction (through the sample). The orange curve in Fig. 20 indicates the simulation that should be compared to the data from “large” nanoprisms on the 500 nm thick α -Si film in Fig. 18.

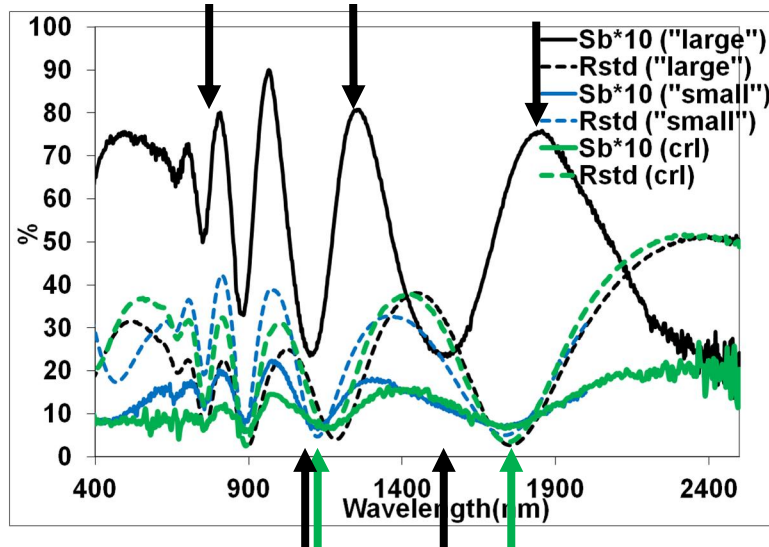


Figure 19: Total integrated backscattering S_b and specular reflectivity R_{std} for nanoprisms and control sample on 500 nm-thick α -Si films. This is the same plot as Fig. 9a, except that the valleys in R_{std} are indicated with upwards-pointing green arrows to indicate maximum transmission, as shown in Fig. 8 for uncoated films of 500 nm α -Si on glass. Indicated peaks (black arrows pointed downwards) and valleys (black arrows pointed upwards) in S_b are: 1.81 μm (the 1st order maximum in S_b), 1.51 μm (the 1st order minimum), 1.25 μm (the 2nd order maximum), 1.06 μm (the 2nd order minimum), and 783 nm (near the 4th order maximum). Data marked "crl" are from control samples.

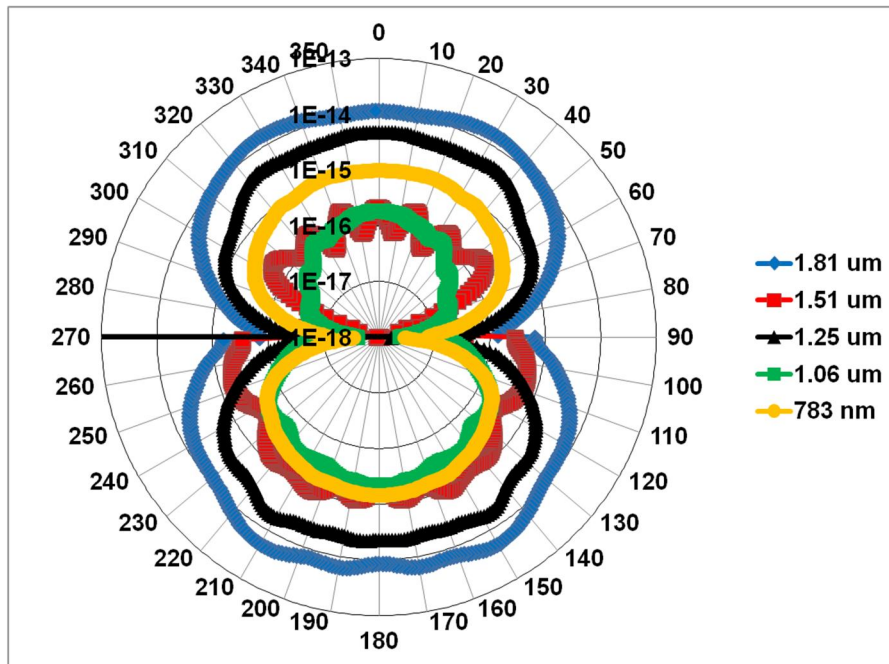


Figure 20: Log scale graph showing FDTD simulations of single-particle scattered power from a 200 nm 40 nm thick Ag nanodisk on 500 nm α -Si film on glass at wavelengths of: 1.81 μm (the 1st order maximum in S_b), 1.51 μm (the 1st order minimum), 1.25 μm (the 2nd order maximum), 1.06 μm (the 2nd order minimum), and 783 nm (near the 4th order maximum). Note that the scattering at wavelengths corresponding to minima of S_b (e.g., 1.51 μm) are primarily in the forward direction ($90^\circ < \theta < 270^\circ$), while scattering at wavelengths corresponding to maxima of S_b (e.g., 1.81 μm) are similar in both the backwards and forward directions. The numbers along the vertical scale bar are arbitrary, but show the correct ratio between scattered power. Longer wavelengths are predicted to scatter more, so curves representing them reach larger values along the radial direction.

The simulations in Fig. 20 show the same rough shape of the scattering profile as a function of angle as the experimental data in Fig. 18. The simulated scattering around 90° and 270° may also be an artifact; because of those very large angles of emission from the sample, the intensity may not be properly extrapolated to the far field. Otherwise, the scattering occurring at wavelengths exhibiting maxima in S_b (e.g., $1.81\ \mu\text{m}$) is fairly uniform with angle, as was observed experimentally (Fig. 18). It is possible that the inhomogeneity in size distribution of the experimental nanoprisms “washes out” the finer features of scattering from individual nanoprisms.

4. CONCLUSIONS

High-quality arrays of Ag nanoparticles (near-spherical SNPs and novel, custom-synthesized nanoprisms) on thin films of α -Si were analyzed in this study. Fabry-Perot resonances of the α -Si thin film complicate the analysis in the optical intermediate field. We observed interesting spectral shifts between total integrated diffuse scattering in the backwards direction (S_b) and the specular reflectivity (R_{std}), and between total integrated diffuse forward scattering (S_f) and specular transmission (T_{std}), in data collected from “large” nanoprism- and 120 nm SNP-coated 500 nm thick α -Si films on glass. These spectral shifts were not as significant for “small” nanoprisms or 50 nm SNPs on 500 nm thick α -Si films, although thinner α -Si films showed shifts in the TIDS signal from “small” nanoprisms. 300 nm SNPs demonstrated very large scattering signatures that masked the specular reflectivity. ARS measurements on nanoprisms on 500 nm thick α -Si films on glass at 780 nm agreed qualitatively with simulations of the scattering from single 200 nm diameter nanodisks also on 500 nm thick α -Si films on glass, although further analysis (different polarizations and laser wavelengths) is suggested. These single-nanodisk simulations predicted that scattering would lie primarily in the substrate (forward scattering) for wavelengths that minimize TIDS, while for wavelengths that maximize TIDS, scattering would be more evenly divided between forward and backwards scattering. Ag nanoparticles with sizes in the range 120 - 800 nm are most promising for enhancing scattering into and absorption in flexible, photovoltaic thin films, and perhaps therefore increasing the short-circuit current density and solar cell efficiency.

5. ACKNOWLEDGMENTS

The Lincoln Laboratory portion of this work was sponsored by the U. S. Army Natick Soldier Research Development and Engineering Center under Air Force Contract FA8721-05-C-0002. Opinions, interpretations, conclusions, and recommendations, from the Lincoln Laboratory portion of the work, are those of the authors, and do not necessarily represent the view of the United States Government.

The MIT ISN authors acknowledge funding from the Army Research Office through the Institute for Soldier Nanotechnologies under Contract No. W911NF-07-D0004.

6. REFERENCES

- ¹ Atwater, H. A. and Polman, A., “Plasmonics for improved photovoltaic devices”, *Nature Materials*, 9 (2010) 205.
- ² Palanchoke, U., *et. al.*, “Plasmonic effects in amorphous silicon thin film solar cells with metal back contacts”, *Optics Express*, 20 (2012) 6340.

³ Diukman, I. and Orenstein, M., “How frontside plasmonic nanostructures enhance solar cell efficiency”, *Solar Energy Materials & Solar Cells* 95 (2011) 2628–2631.

⁴ Pala, R., *et. al.*, “Design of plasmonic thin-film solar cells with broadband absorption enhancements”, *Advanced Materials* 21 (2009) 3504-9.

⁵ Kinnan, M. K., Kachan, S., Simmons, C. and Chumanov, G., “Plasmon Coupling in Two-Dimensional Arrays of Silver Nanoparticles - I. Effect of the Dielectric Medium” *J. Phys. Chem. C* 113 (2009) 7079-84 and Kinnan and G. Chumanov, “Plasmon Coupling in Two-Dimensional Arrays of Silver Nanoparticles: II. Effect of the Particle Size and Interparticle Distance”, *J. Phys. Chem. C* 114 (2010) 7496.

⁶ Gan, Q., Bartoli, F. and Kafafi, Z., “Plasmonic-enhanced organic photovoltaics: breaking the 10% efficiency barrier”, *Advanced Materials* 25 (2013) 2385.

⁷ Singh Gill, H. and Kumar, J., private communication (2014).

⁸ Sablon-Ramsey, K., *et. al.*, “Subwavelength nanostructures integrated with polymer packaged solar cells for omnidirectional broad spectrum improvement of photovoltaic performance”, submitted to *Adv. Energy Sciences* (2014).

⁹ Yang, Y., *et. al.*, “Multiple shape Ag nanoparticles for SERS”, *J. Phys. Chem. C* 111 (2007) 9095.

¹⁰ Palik, E. “Handbook of Optical Constants of Solids” (2007).